Indian Journal of Marine Sciences
Vol. 37(1), March 2008, pp. 13-34

Interannual variability of the South Indian Ocean in observations and a coupled model

Bohua Huang* & J. Shukla

Department of Climate Dynamics, College of Science, George Mason University, Virginia, USA
Center for Ocean-Land-Atmosphere Studies, Institute of Global Environment and Society, Maryland, USA
*[E-mail: huangb@cola.iges.org]

The mean state, annual cycle, and interannual variability of the coupled ocean-atmosphere in the South Indian Ocean produced by a 300-year simulation of a coupled ocean-atmosphere general circulation model (CGCM) are compared with those from 51-year (1950-2000) observational datasets. The CGCM simulates realistically the mean annual cycles for both the sea surface temperature (SST) and lower atmospheric circulation, including the seasonal positions of the 10°C and 20°C SST isotherms, the zonal and meridional migration of the South Indian Ocean subtropical high, and the fluctuation of the southeast trade winds and mid-latitude westerly winds.

Interannually, the dominant model anomalous SST pattern in austral summer and fall showed some similarities to the observed Indian Ocean subtropical dipole mode, featuring opposite SST anomalies between the northeastern ocean to the west of Australia and the southern ocean. The model pattern is different from the observed one in its overly zonal spatial structure. Both the model and observed anomalous events are generated in response to atmospheric perturbations over the subtropical and mid-latitude South Indian Ocean that disturb the subtropical high during austral spring and summer. The corresponding wind speed changes of the trade winds and westerly modulate the surface heat flux into the ocean and generate SST anomalies, which usually persist into austral fall and in turn modify the lower atmospheric circulation in the subtropical Indian Ocean, especially the areas near Madagascar in the fall season. In the observations, the initial extratropical atmospheric fluctuations are significantly correlated to the global tropical variations associated with El Niño/Southern Oscillation. They are more strongly linked to the southern annular mode in the model.

[**Key words:** South Indian Ocean, air-sea interaction, interannual variability, coupled ocean-atmosphere general circulation model]

1. Introduction

The strongest interannaul variability of the sea surface temperature (SST) in the Indian Ocean appears in the southern subtropical-extratropical region (20°S-50°S), where the standard deviations of the seasonally averaged SST anomalies surpass 0.4°C in large areas across the basin[1]. The enhanced SST fluctuation in the subtropical-extratropical open ocean is part of a universal feature of the Southern Oceans[1]. These SST fluctuations affect regional climate variability significantly. Mason[2] found that warmer SST in the southwestern Indian Ocean is associated with wetter conditions over the eastern and central South Africa in austral summer. Using an atmospheric general circulation model (AGCM) forced with an idealized warm SST pattern planted in the southwestern Indian Ocean, Reason & Mulenga[3] showed that these SST anomalies could induce moist convergence and excessive precipitation over the continent. The rainfall over the African continent is also sensitive to the location of the SST anomalies within the South Indian Ocean. Rocha & Simmonds[4] noticed that a warming in the central Indian Ocean weakens the low-level easterlies toward the African coast and thus reduces the moisture entering the continent. Near the eastern boundary, Nicholls[5] found that an anomalous winter (June-August) rainfall band stretching from the northwest to southeast Australia is connected to the SST difference between the Indonesian region and the central Indian Ocean. England *et al.*[6] also linked the interannual rainfall extremes over the southwest tip of the western Australia to the SST anomalies of opposite centers near the western coast of Australia and the western Indian Ocean. They pointed out that this SST pattern

*Corresponding author:
Dr. Bohua Huang, Center for Ocean-Land-Atmosphere Studies, Institute of Global Environment and Society, 4041 Powder Mill Road, Suite 302, Calverton, MD 20705. Phone: (301) 5957000; Fax: (301) 5959793; [E-mail: huangb@cola.iges.org].

bears certain resemblance to the one previously shown by Nicholls[5].

A comprehensive view about the large-scale anomalous SST patterns in the South Indian Ocean is necessary to explain these SST-rainfall relations. Through an empirical orthogonal function (EOF) analysis, Behera & Yamagata[7] found that the SST anomalies in the subtropical South Indian Ocean is characterized as a basin-wide dipole pattern with opposite poles off Australia and south of Madagascar, which is usually referred to as the Indian Ocean subtropical dipole (IOSD) mode. They demonstrated that the IOSD mode is phase-locked to austral summer and generated by surface latent heat flux changes associated with the wind speed fluctuations. On the other hand, the SST pattern identified by England *et al.*[6] from western Australian precipitation does not coincide with the IOSD mode both spatially and temporarily, even though a somewhat similar thermodynamic generation by the subtropical anticyclone over the South Indian Ocean seems to be at work. A possible explanation of this discrepancy is that these two SST patterns prevail in different seasons. Regardless the seasonality, the thermodynamic nature of the subtropical-extratropical SST fluctuation is distinctive of the more famous tropical Indian Ocean dipole (IOD) mode[8], which is mainly associated with the dynamic air-sea feedback involving the oceanic thermocline[9-12].

Some modeling studies have examined the IOSD mechanisms. Suzuki *et al.*[13] examined the simulated IOSD in a coupled ocean-atmospheric general circulation model (CGCM). The model IOSD events are depicted from a subtropical dipole index (SDI) based on a visual inspection of the raw data, which is defined as the SST anomaly difference between the western (30°-42°S, 50°-80°E) and eastern (17°-29°S, 75°-105°E) nodes. Their composites of these major events showed that the CGCM is able to simulate quite realistically the evolution of the observed IOSD events. In a CGCM study that was more concentrated on the tropical-subtropical Indian Ocean, Huang & Shukla[14] identified a major EOF mode of the model SST anomalies in the Indian Ocean to the north of 30°S, which has a dipole-like structure centered in the subtropical Indian Ocean. They showed that this pattern is generated by the surface heat flux anomalies. Although these CGCM studies demonstrated that the observed IOSD mechanism works in the models, the strength of the model IOSD pattern is yet to be evaluated. In this aspect, an objective statistical analysis of the subtropical-extratropical ocean is needed.

It is also not clear whether these SST anomalies are sporadically generated by random local atmospheric fluctuations or connected to global climate variations. Physically, the origin of the SST fluctuation in the subtropical Indian Ocean may be complicated due to the interference of the tropical and extratropical influences in this region. In addition to the oceanic Rossby waves from tropics, which are indirectly linked to the El Niño events[9-10], El Nino/Southern Oscillation (ENSO) may also directly generate atmospheric wave train into the South Indian Ocean domain[15]. Analyzing observations and a CGCM simulation, Lau & Nath[16] found that, in austral winter, a zonally elongated sea level pressure (SLP) anomaly located to the south of Australia can induce dipole-like SST anomalies in the tropical Indian Ocean. The anomalous SLP is linked to the southern annular mode (SAM)[17], an opposite SLP fluctuation between the mid-latitude and polar zones. Huang & Shukla[14] also found that SAM is responsible for the subtropical dipole SST pattern in their CGCM simulation during austral summer and fall. To evaluate the predictability of the SST variability, its connection to these global-scale climate variations needs to be clarified.

In this paper, we examine the interannual SST variability in the South Indian Ocean using both observational datasets and a long-term CGCM simulation. Given the constraint of the paper's length, we will concentrate on the IOSD pattern in austral summer and fall. The reader can find the study area of this paper in the oceanic domain in Figure 1. For both the model and observations, the dominant patterns of the SST variability in the subtropical-extratropical South Indian Ocean are identified using the same objective statistical method. The connections between the ocean and the lower atmosphere are also determined statistically. The regional air-sea processes are then linked to the global-scale climate variations. In fact, we would like to emphasize the difference between the model and the observations in their global connections.

2. Methodology

In this study, we use the extended reconstruction of the monthly mean global SST analysis (ERSST, version 2)[18] for 1950-2000. The SST analysis is on a 2° latitude × 2° longitude grid, produced from the

latest version of the Comprehensive Ocean-Atmosphere Data Set (COADS). Compared to other SST analyses from the US Climate Prediction Center, the ERSST extends its coverage to most of the Southern Ocean. The corresponding atmospheric monthly mean data for the same period are from the National Centers for Environment Predictions (NCEP) and National Center for Atmospheric Research (NCAR) meteorological reanalysis[19]. Monthly anomalies are defined as departures from the climatological monthly means of the 51-year record. These monthly anomalies are then averaged to form seasonal means for December-February (DJF), March-May (MAM), June-August (JJA), and September-November (SON), corresponding to austral summer, fall, winter, and spring respectively. From now on, seasons are based on the austral calendar. All seasonal data are detrended by eliminating a linear local trend. This procedure eliminates a long-term tendency in the reanalyzed sea level pressure (SLP) fields. The existence of such a trend needs further validation because of the potentially large errors in the reanalyzed SLP in mid and high latitudes of the southern hemisphere[20], which is beyond the scope of the present study.

The atmospheric component[21] of the CGCM is a global spectral AGCM with a triangular truncation of the spherical harmonics at T42. Vertically, it is divided into 18 σ levels with higher resolution in the lower troposphere. The model has the same dynamical core as that of the NCAR Community Climate Model (version 3.0). Its subscale physical parameterization is state-of-the-art. The oceanic GCM (OGCM) is a quasi-isopycnal model of 14 active layers[22]. Its domain is the World Oceans within 70°S-65°N with a horizontal resolution of 1° latitude × 1.25° longitude while the meridional resolution is increased to 0.5° within 10°S-10°N. The 1st model layer represents the oceanic mixed layer with the entrainment at its base calculated following Niiler & Kraus[23]. The vertical mixing below the mixed layer is dependent on the Richardson number. The coupling between the OGCM and the AGCM is on a daily interval. The globally coupled model is integrated for 500 years with initial conditions derived from long-term uncoupled simulations. The last 300-year simulation of the CGCM is used in this study. Relevant model outputs are processed to derive the mean monthly climatology and seasonal anomalies in the same way as described for the observations.

The empirical orthogonal function (EOF) technique is used to objectively identify the dominant patterns of the SST anomalies and other variables in the South Indian Ocean for the CGCM and the observations. Considering the strong phase-lock of the SST anomalies with the normal annual cycle, the EOF analysis is conducted on a season-by-season basis. To further study the connection between the ocean and atmosphere, a canonical correlation analysis (CCA) is conducted between the seasonal mean SST and SLP anomalies in the region. CCA is a statistical technique to identify spatial patterns from two fields, which optimizes the correlation coefficient between their corresponding temporal expansion coefficients. In this application, we follow the approach of Barnett & Presendorfer[24] of filtering each field by projecting the raw data onto the 10 leading EOFs. In all cases, the filtered data explain above 80% and 90% of the total variances for the model and observations respectively. The benefit associated with the pre-filtering is discussed in Bretherton *et al.*[25], among others. Correlation and regression analyses between the time series of the leading EOF SST patterns and other major climate indices are calculated to establish their statistical connections. To examine the temporal-spatial evolutions of these dominant patterns, a composite analysis is conducted using the strong anomalous events selected from the amplitudes of the EOF time series. The selection procedure will be described later using a real time series as example.

3. Mean state and annual cycle

Figure 1 shows the seasonal means of the climatological SST field of the Indian Ocean from the equator to 60°S for the observations and the CGCM simulation. The observed SST is characterized by southward decrease with the strongest gradient appearing near 30°S and between 40°-50°S, corresponding to the oceanic subtropical convergence and the polar front zone. The isotherms between 20°-40°S are slightly tilted from southwest to northeast, with their most northern positions near 100°-105°E. Close to the western Australian coast, however, the isotherms tilt southeastward because the Leeuwin current carries warm water southward.

An annual cycle is clearly seen from the enlarged area bordered by the 28°C isotherm from winter-spring (Fig.1A, B) to summer-fall (Fig.1C, D) in the tropics, as well as the southward migration of the 20°C isotherm in the same period, which moves from

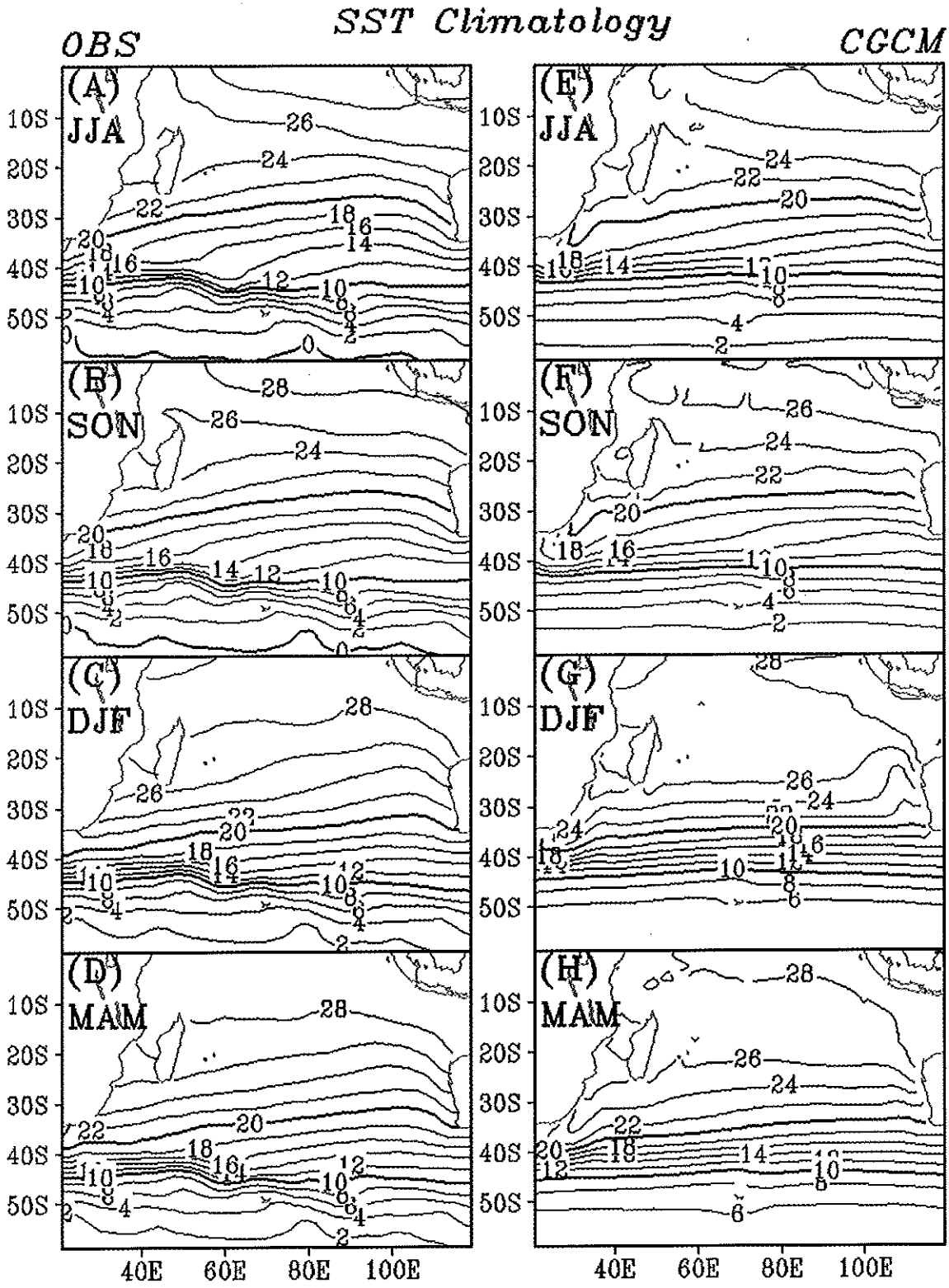

Fig. 1—Seasonally averaged climatological SST in the South Indian Ocean for 1950-2000 from the ERSST (A-D) and a 300-year CGCM simulation (E-H). The seasonal averages are shown with the 1st row for austral winter (JJA), the 2nd row for spring (SON), the 3rd row for summer (DJF), and the 4th row for autumn (MAM). For all panels, the contour interval is 2°C with the 10°C and 20°C isotherm highlighted.

around 30°-35°S in winter-spring (Fig.1A, B) to about 35°-40°S in summer-fall (Fig.1C, D). On the other hand, the 10°C isotherm is nearly stationary at round 40°S throughout the year, although the water temperature also rises for about 2°C from winter to summer. Due to the southward migration of the 20°C isotherm, the meridional SST gradient is tightened up around 40°S in DJF and MAM.

The CGCM reproduces these observed features qualitatively, in particular the positions of the 10° and 20°C isotherms as well as the substantial migration of the latter with season (right panels). So is the enhancement of the meridional SST gradient near 40°S in summer and fall. A major shortcoming of the simulation is its excessively warm surface water to the south of 50°S in summer and fall when the model SST in this zone is between 4°-6°C uniformly while the observed SST is still below 2°C in the south (Fig.1C, H). Due to this difference, the amplitude of the SST annual cycle is apparently larger in the model than in the observations at higher latitudes. This is possibly due to the lack of interactive sea ice in the model so that the increased surface heat flux in summer raises water temperature instead of melting sea ice. While the origin of this error is at higher latitudes, its effect is visible in the southern part of the domain we consider.

The South Indian Ocean SST is closely linked to the overlaying atmosphere. Figure 2 shows the seasonal averaged SLP climatology for the observations and CGCM, superimposed with the corresponding surface wind stress over the ocean. The regional atmospheric circulation is dominated by the Indian Ocean subtropical high (or Mascarene High[26]), with southeasterly trade winds in its northern flank and the westerly belt to its south. In the observations, a high-pressure belt of 1020 hPa extends from the African continent toward the eastern Indian Ocean between 20°S-35°S in JJA (Fig.2A). Its center of pressure above 1023 hPa is located at 30°S over the central-western ocean. The SLP in this region decreases during the next two seasons, forming a closed 1020 hPa contour line, which first occupies most of the subtropical ocean in SON (Fig. 2B) then shrinks to the southeastern part of the basin. This movement of the high-pressure center generates corresponding migration of the westerlies in the south and the trade winds in the north. In particular, the enhanced trade winds over the ocean near the western coast of Australia (Fig. 2C) cause the tilting the isotherms (Fig. 1C) by cooling down the sea surface in this region. The high pressure starts to increase and expand westward in MAM (Fig. 2D).

The CGCM also reproduces this annual cycle of the Mascarene high qualitatively, including its seasonal enhancement and migration. Quantitatively, the model pressure at the center of its subtropical high is generally higher than that of the observations, except for DJF (Fig. 2G). In the model, the zonal movement of the subtropical high is also wider, with its center located over the African continent in JJA (Fig.2E) while closer to the coast of Australia in DJF (Fig.2G) than the observations (Fig.2C). This explains the apparent excursion of the isotherms near the eastern boundary in the model SST field during DJF (Fig.1G). The other major model discrepancy from the observations is the overly strong meridional SLP gradient between 40°S-60°S, especially during winter and spring. In the tropics, the model simulates the northward cross-equatorial flow successfully during the Indian Monsoon season (Fig.2A, E). However, an excessive southward flow passes through the equator along the Somali coast in the model during DJF, which generates a weak artificial cyclone between 10°S-20°S east of Madagascar (Fig.2G).

In spite of these quantitative differences, the CGCM simulates the major features of the mean state and annual cycle of the South Indian Ocean SST and the lower atmospheric circulation realistically. Similar to what has been described by Huang & Shukla[27] for the subtropical North Atlantic Ocean, beside the seasonal forcing that mainly influences the meridional migration of the subtropical high, the zonal migration of the subtropical high center with season in the South Indian Ocean may partly result from a coupled feedback between the SST and the subtropical anticyclone. The wind speed change associated with the migration of the subtropical anticyclone in the summer cools the sea surface in the east. The cold SST in turn increases the local pressure and draws the anticyclone further east. This feedback process is likely sustained in the annual cycle in the CGCM. In the rest of this paper, we examine whether similar processes can affect the air-sea anomalies superimposed on this normal annual cycle.

4. Leading interannual patterns

4.1 EOF analysis

Figure 3 shows the spatial patterns of the 1st EOF modes of the seasonally averaged SST anomalies calculated for the oceanic domain within 10°S-50°S,

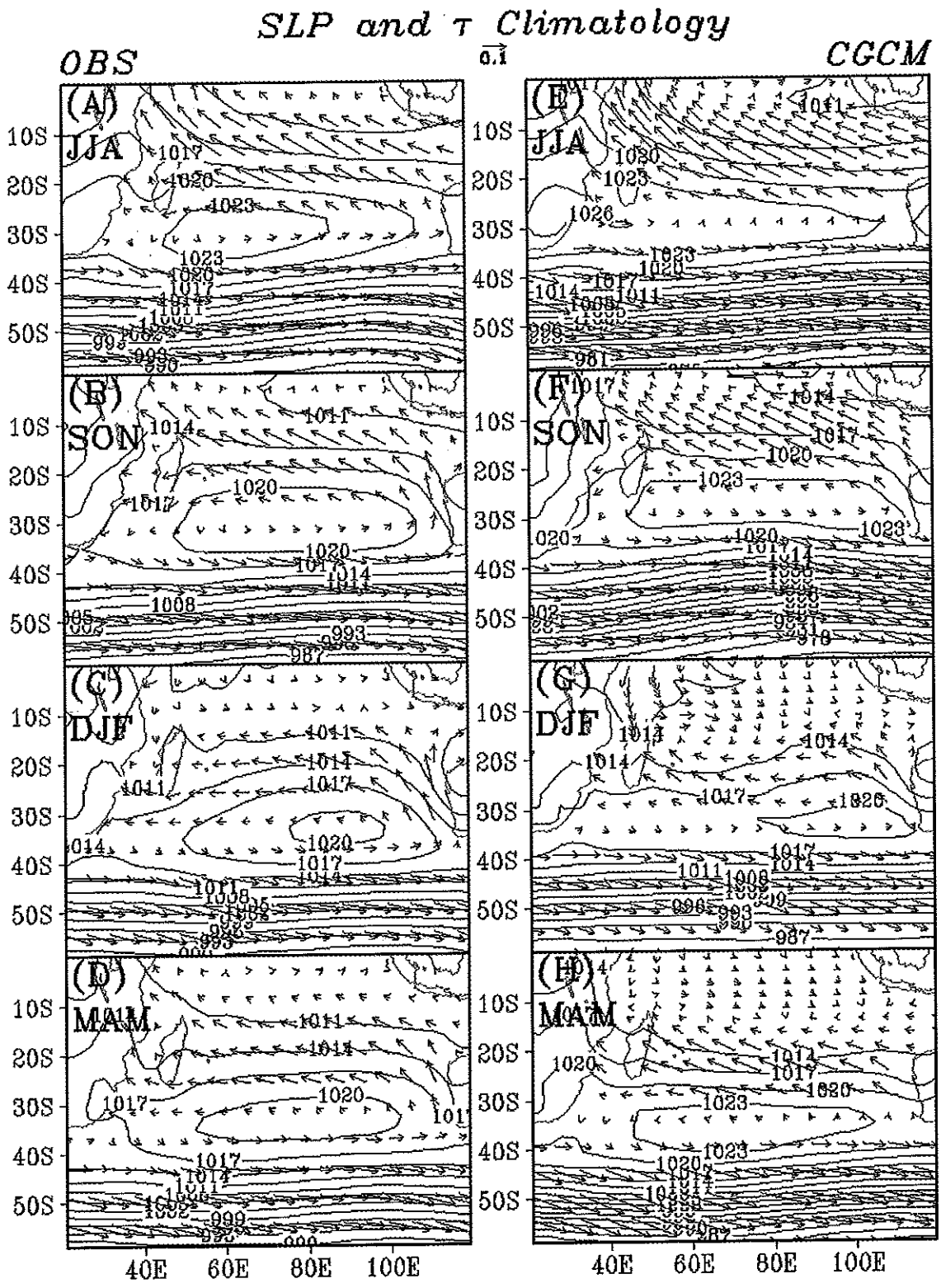

Fig. 2—Seasonally averaged climatological sea level pressure (SLP) and the surface wind stress over the South Indian Ocean domain for 1950-2000 (A-D) from the NCEP/NCAR reanalysis and a 300-year CGCM simulation (E-H). The seasonal averages are shown with the 1st row for austral winter (JJA), the 2nd row for spring (SON), the 3rd row for summer (DJF), and the 4th row for autumn (MAM). For all panels, the contour interval for SLP is 3hPa. The scale of the wind stress vector with magnitude 0.1Nm^{-2} is at the top center.

30°E-120°E. The two upper panels give the EOF patterns from the 51-year observations for DJF (Fig.3A) and MAM (Fig.3B) respectively, while the lower two panels (Fig.3C, D) show the corresponding ones from 300-year CGCM simulations. The observed SST EOF mode in DJF (Fig.3A) is characterized by a tilted dipole pattern of opposite anomalies, with its southwestern node at 45°S, 60°E and northeastern node at 25°S-30°S, 90°E-100°E. Compared to the southern branch, the northern one is elongated northwestward to the northern tip of Madagascar. The EOF pattern in MAM (Fig.3B) is qualitatively similar.

There are significant differences between the patterns from the model (Fig.3C, D) and observations (Fig.3A, B), although the CGCM EOF mode in DJF (Fig.3C) shows a dipole between the warm anomaly expanding northwestward from the western Australia and the cooling further to the south in mid-latitude, which is similar to the observations (Fig.3A). Compared to the observations (Fig.3A), the model pattern (Fig.3C) is more zonally oriented, especially the elongated cold center that is stretched eastward. Moreover, the meridional scale of the model pattern is apparently narrower. There is also an additional sign change between 40°S-45°S that is not observed. The westward movement of the mid-latitude cold center in MAM (Fig.3D) seemingly brings the model pattern slightly closer to its observed counterpart in the mid-latitude (Fig.3B). However, the discrepancy is still quite large in the higher latitudes. In the tropics, the weakening of the model warm branch in the east and the expansion of the cold one in the west (Fig.3D) also deviate significantly from the observations (Fig.3B) significantly.

Apart from the similarity in spatial structures, the two independently derived EOF modes in DJF and MAM also show significant coherence temporarily. This is the case for both the observations and the model. The time series (principal component, or PC) of the DJF EOF is correlated to the subsequent MAM PC at 0.73 for the observations and 0.74 for the CGCM, which suggests a strong persistence from summer to fall. The PCs of these leading EOF modes are also highly correlated to the IOSD index defined by Suzuki *et al.*[13] in their respective seasons. In the observations, the correlations are 0.91 and 0.93 for DJF and MAM respectively. The corresponding ones from the CGCM are 0.81 and 0.72. Considering the

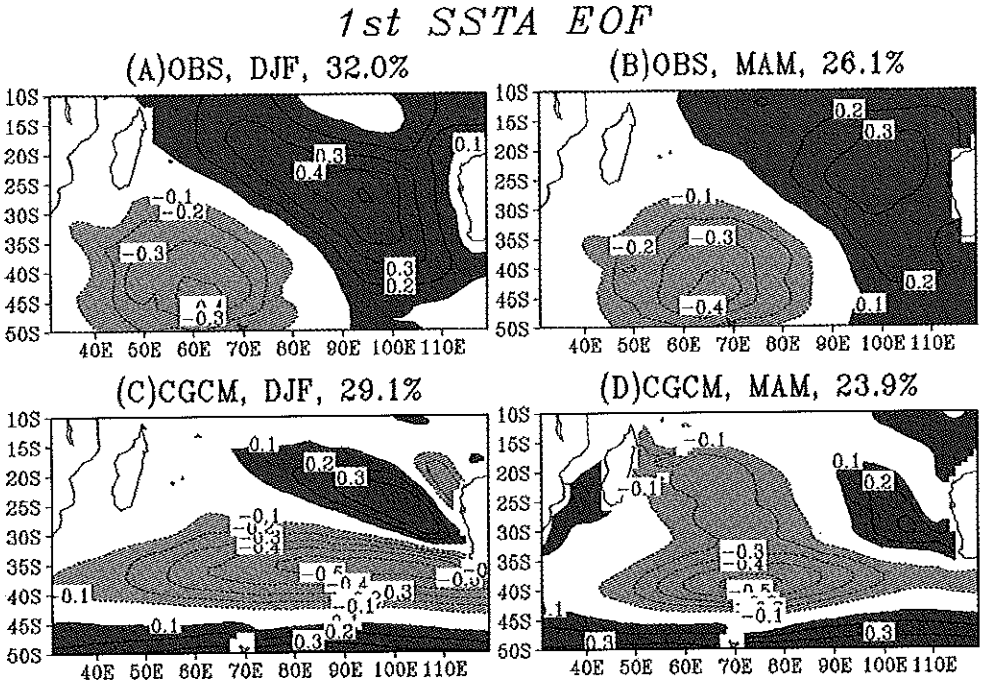

Fig. 3—The 1st EOF modes of the seasonally averaged SST anomalies from the observations for 1950-2000 in (A) DJF and (B) MAM. Their CGCM counterparts from a 300-year simulation are shown in (C) and (D) respectively. The percentage of total variance explained by each mode is shown at the top of each panel. Since the principal components of these EOF modes are normalized, the magnitude of the loadings is comparable to the local standard deviation. For all panels, the contour interval is 0.1°C with zero contours omitted. Areas with loading larger than 0.1°C are darkly shaded and those less than –0.1°C are lightly shaded.

much larger model sample size, these numbers, though somewhat lower than the observed, are still very robust. The regressions of the seasonal mean data to these indices actually recover the EOF patterns shown in Fig.3. Therefore, the IOSD index is a good characterization of these objectively determined modes.

We have also calculated the EOF modes of the seasonally averaged SLP anomalies in the same latitude-longitude domain (not shown). For both the model and the observations, the 1st modes show the nearly zonal belts of opposite anomalies between the mid and high latitudes, which is apparently the signature of SAM. The 2nd modes, on the other hand, depict the vortex circulation in the mid latitudes. Though with qualitative similarity, a major difference between the model and the observations is that, SAM is much stronger in the model.

4.2 CCA patterns

To link the SST and SLP anomalies in the South Indian Ocean, the leading CCA patterns between these two variables are examined. The domain of the SST field for CCA is the same as the one for EOF analysis. The domain for SLP is extended to cover the region within 20°E-150°E, 10°S-70°S. Given the strong persistence of the SST patterns from DJF to MAM, our emphasis is concentrated on the preceding season (DJF) of the two because it tells more about the generation of these patterns.

Figure 4 shows the 1st CCA mode between the observed SST and SLP anomalies in DJF. The spatial patterns of the SLP (Fig.4A) and SST (Fig.4B) anomalies are closely connected to each other in this mode, as demonstrated by their highly coherent time series with a correlation coefficient 0.94. The abscissa in Fig.4C marks the year when a DJF season starts. The SST pattern is also consistent with the independently derived EOF mode in spatial structure (Fig.3A). The correlation between their corresponding time series is 0.92. Therefore, the SST pattern derived from CCA is nearly indistinguishable from the leading EOF mode.

The SLP pattern is characterized by a mid-latitude low pressure over the ocean, centered at 50°S, 70°E (Fig.4A) and a high pressure center over the western Australia, which extends northwestward into the tropical Indian Ocean and southward along 110°E. A secondary low can also be seen in the mid-latitude further to the east. It is interesting to note that the SST dipole pattern is located in between the centers of the opposite two SLP poles in the Indian Ocean-Australia sector (Fig.4A, B). This relationship is consistent with the scenario discussed in previous studies, i.e., the wind speed anomalies associated with the strong SLP gradient drive the anomalous SST pattern[7,14]. Therefore, the establishment of the anomalous SLP centers over the South Indian Ocean and Australia plays a key role in generating the subtropical dipole SST pattern.

In the CGCM, however, a quite different SST-SLP relation is established. The leading CCA pattern for the SST anomalies in DJF (Fig.5B) is nearly the same as the EOF mode (Fig.3C) with their time series correlated at 0.90. Its corresponding SLP pattern features opposite anomalies between the mid-latitude zone (30°S-50°S) and the areas further south, which is the typical regional structure of SAM. One should notice that a larger contour interval is used to plot the anomalous SLP pattern in Fig.5A (0.5hPa) than in Fig.4A (0.2hPa), which can be used as an indicator of the intensity difference between the two modes. The correlation level between the model SST and SLP patterns is high for the CGCM mode (Fig.5C). It is noticeable that the mid-latitude low-pressure zone in Fig.5A has a regional center in the South Indian Ocean, which is roughly in the same location as the low pressure in Fig.4A. The enhanced SLP gradient in the northwestern side and to the south of the low-pressure center generates the corresponding centers of the SST pattern (Fig.5B). However, the opposite SLP anomalies centered over Australia are totally missed by the model. Therefore, the forcing mechanism of the IOSD pattern in the model is significantly different from that in the observations.

4.3 Global connection

To examine the potential links of these regional coupled patterns to the larger-scale variability, the CCA time series for each variable is correlated globally with its original data for both the SLP and SST anomalies over a broader domain (Figures 6 and 7). Figure 6A shows the correlation pattern for the observed SLP anomalies. Apart from the regional correlation between the South Indian Ocean and Australia, significant correlations also occur in the Pacific and Atlantic basins. In the Pacific Ocean, the opposite correlations between the broad area in the western Pacific and eastern Indian Ocean centered in Australia and the equally large regions centered in the

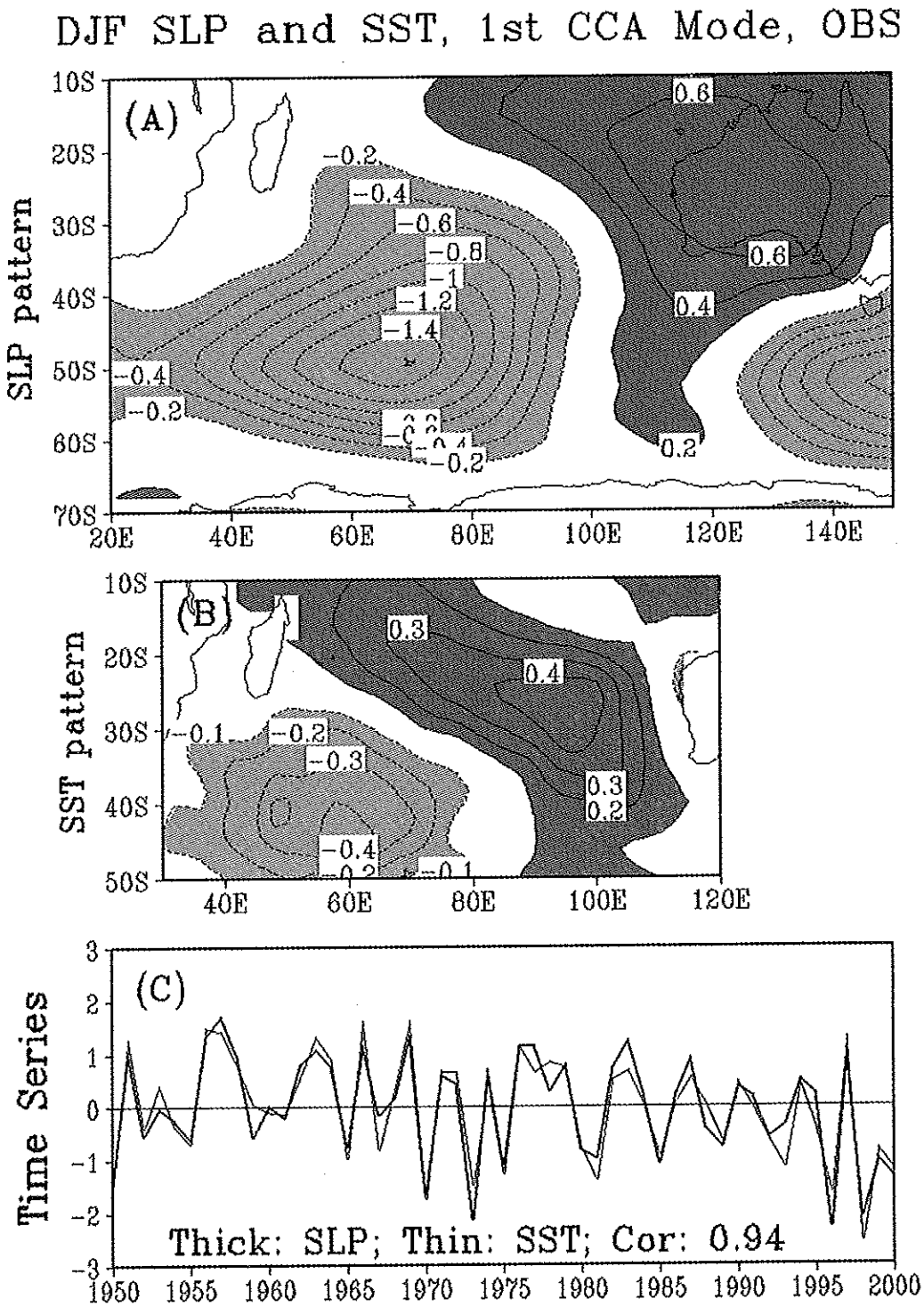

Fig. 4—The 1st CCA mode between the seasonally averaged SLP and SST anomalies for DJF from the observations in 1950-2000. The upper and middle panels show the spatial patterns for (A) the SLP and (B) SST anomalies respectively. The lower panel gives the normalized time series of the SLP (thick curve) and SST (thin curve) respectively. The abscissa in (C) marks the year when a DJF season starts. Also shown in this panel is the correlation coefficient between the two time series. For the upper two panels, the contour interval is 0.2 hPa in (A) and 0.1°C in (B). The zero contours are omitted in both panels. The areas with SLP anomalies larger than 0.2 hPa (SST anomalies larger than 0.1°C) are darkly shaded while those less than –0.2 hPa (or –0.1°C) are lightly shaded.

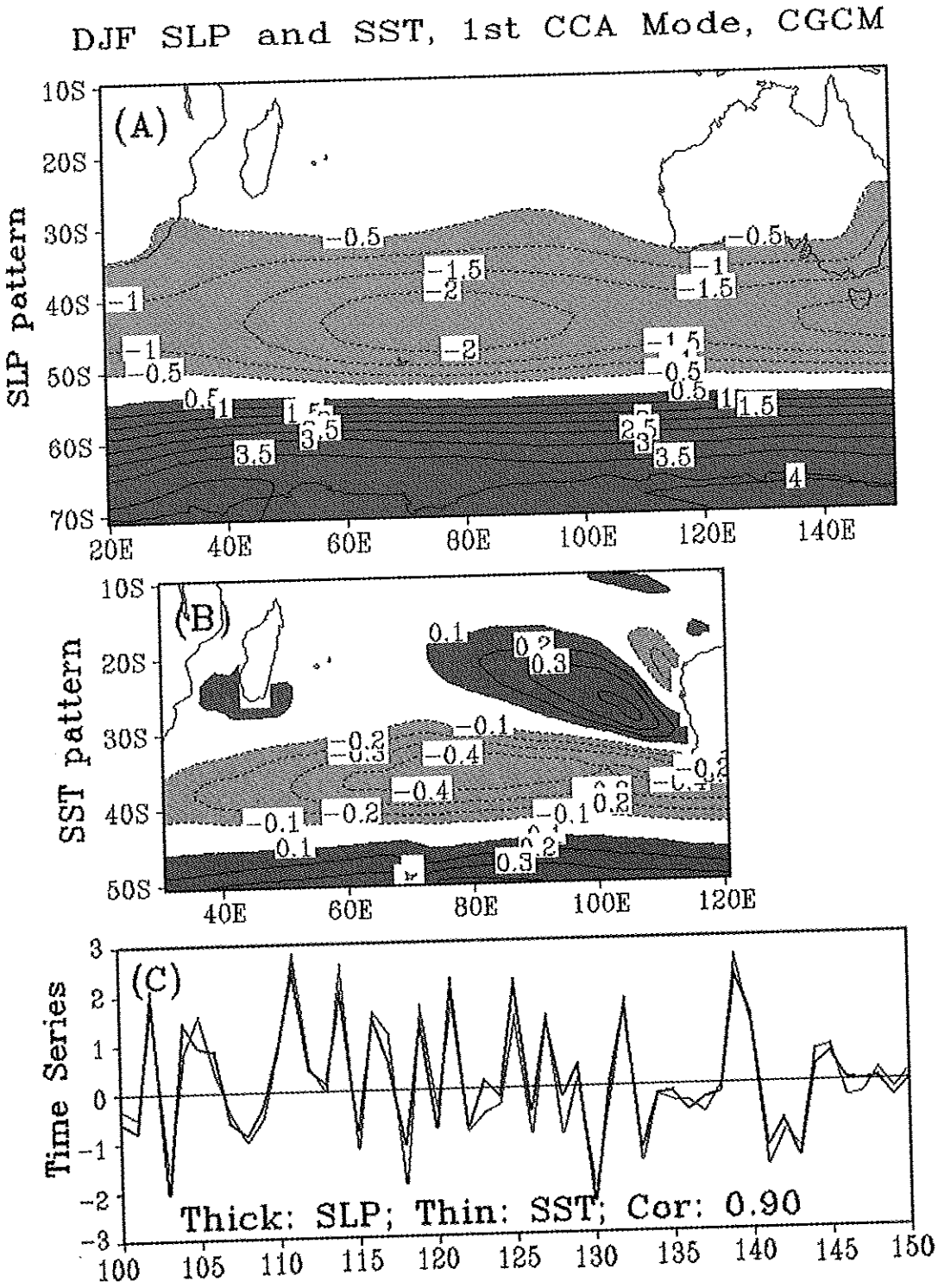

Fig. 5—The 1st CCA mode between the seasonally averaged SLP and SST anomalies for DJF from the 300-year CGCM simulation. The upper and middle panels show the spatial patterns for (A) the SLP and (B) SST anomalies respectively. The lower panel gives a 51-year segment of the 300-year normalized time series of the SLP (thick curve) and SST (thin curve) respectively. The abscissa in (C) marks the year when a DJF season starts. Also shown in this panel is the correlation coefficient between the two time series. For the upper two panels, the contour interval is 0.5 hPa in (A) and 0.1°C in (B). The zero contours are omitted in both panels. The areas with SLP anomalies larger than 0.5 hPa (SST anomalies larger than 0.1°C) are darkly shaded while those less than –0.5 hPa (or –0.1°C) are lightly shaded.

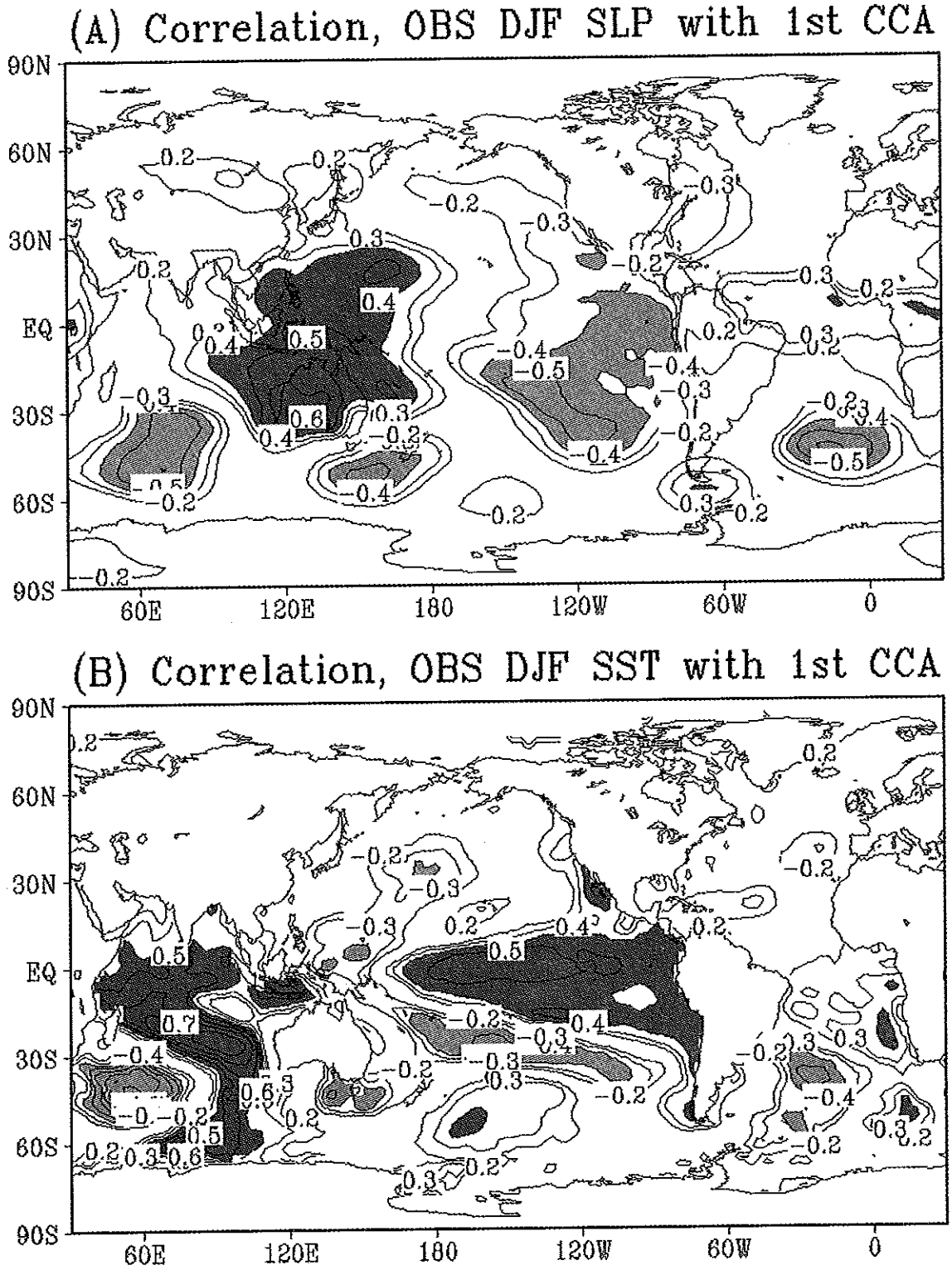

Fig. 6—(A) Correlation coefficients between the SLP time series of the observed 1st SLP-SST CCA mode in DJF and the seasonally averaged SLP anomalies for 1950-2000. (B) Correlation coefficients between the SST time series of the observed 1st SLP-SST CCA mode in DJF and the seasonally averaged SST anomalies for 1950-2000. The contour interval is 0.1 with zero and ±0.1 contours omitted. Areas larger than 0.4 (less than –0.4) are darkly (lightly) shaded.

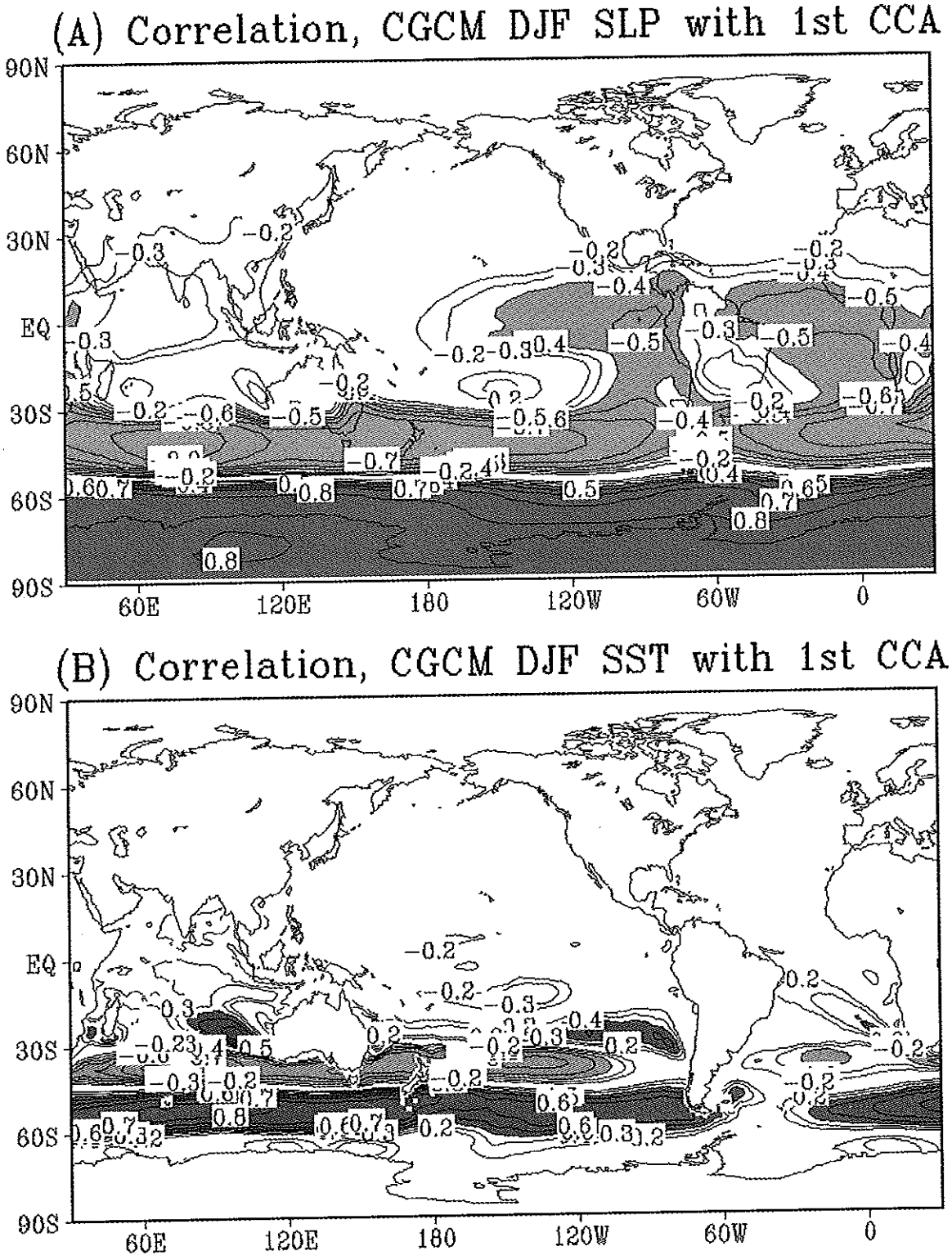

Fig. 7—(A) Correlation coefficients between the SLP time series of the CGCM 1st SLP-SST CCA mode in DJF and the seasonally averaged SLP anomalies for a 300-year simulation. (B) Correlation coefficients between the SST time series of the CGCM 1st SLP-SST CCA mode in DJF and the seasonally averaged SST anomalies for a 300-year simulation. The contour interval is 0.1 with zero and ±0.1 contours omitted. Areas larger than 0.4 (less than –0.4) are darkly (lightly) shaded.

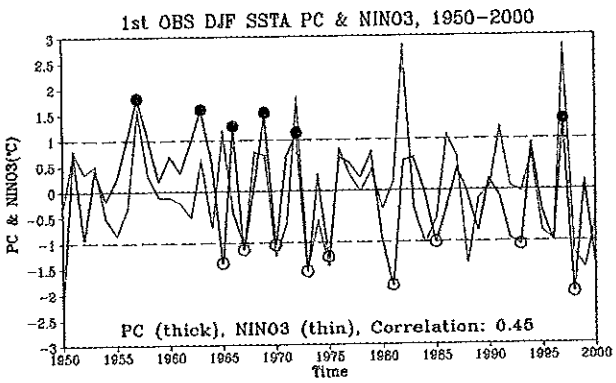

Fig. 8—The thick curve shows the principal component (PC) of the 1st EOF mode for the seasonally averaged observational SST anomalies in DJF. The abscissa marks the year when a DJF season starts. The time series is normalized to have unit standard deviation. The solid and open circles denoted on the local peaks of this curve represent the chosen major positive and negative events for composite analysis. The thin curve shows the NINO3 index (SST anomalies averaged within 5°S-5°N, 90°W-150°W, unit °C) for the same season. The two dashed horizontal lines give the one-standard-deviation limits for the PC. The correlation coefficient between the PC and NINO3 index is given at the lower right corner of the figure.

fluctuations from higher latitudes, such as SAM. These stimulating differences explain some differences in the structures of the observed and model SST patterns.

5. Composite analysis

To further understand the large-scale ocean-atmosphere circulation patterns associated with the South Indian Ocean SST anomalies in summer and fall, a composite analysis of major events is conducted for various variables. The anomalous events chosen for composite are based on the PCs of the DJF SST anomalies for the observations (Fig.3A) and the model (Fig.3C). Here we use the PC of the 1st EOF mode of the observed DJF SST anomalies (thick curve, Fig.8) to explain the two criteria used for the selection. As before, the abscissa in figure 8 marks the year when a DJF season starts. First, the PC magnitude should be larger than its standard deviation marked by the two long dashed horizontal lines in Fig.8. Second, all the chosen years should be local peaks (maxima or minima) of the PC time series.

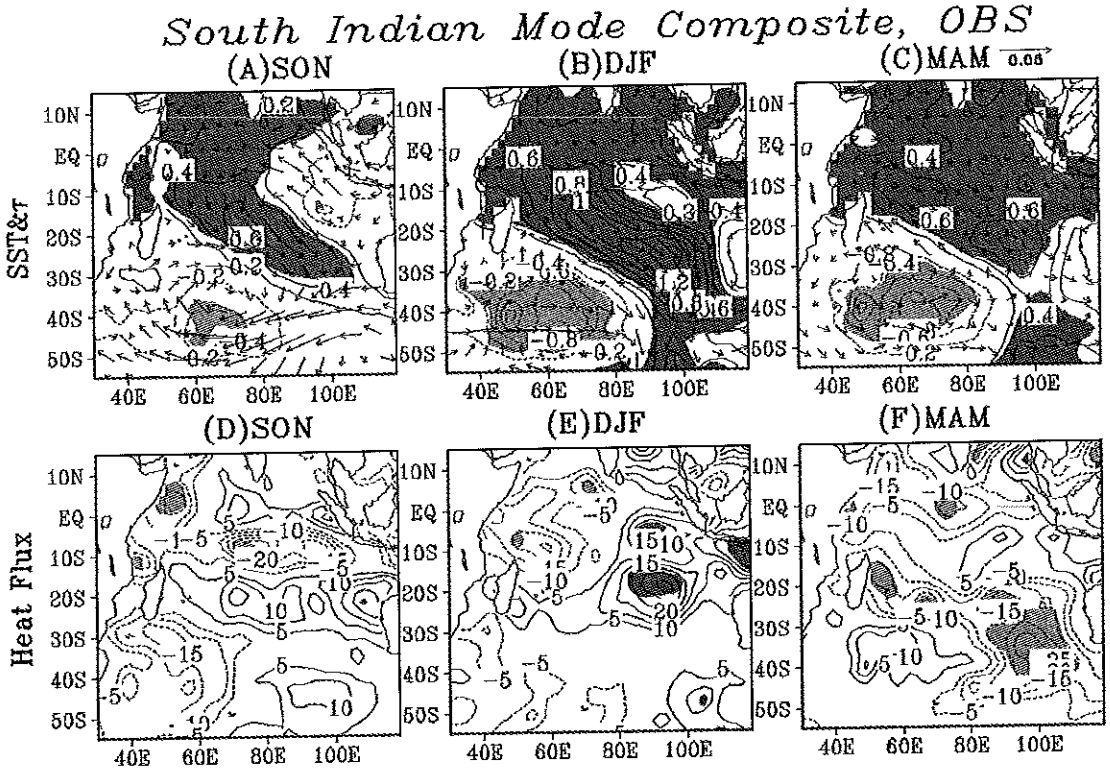

Fig. 9—The composite South Indian Ocean anomalous event formed by the difference between the observed six positive and nine negative events for the SST and wind stress anomalies (A-C) and surface heat flux anomalies (D-F). The sequence of composites is from SON (A, D), to DJF (B, E), then to MAM (C, F). The contour intervals are 0.2°C for the SST anomalies and 5 Wm^{-2} for the surface heat flux anomalies, both with zero contours omitted. The wind stress vector magnitude of 0.05Nm^{-2} is shown at the top right of panel (C). Regions with the differences of the SST or heat flux anomalies above 95% significance level are shaded.

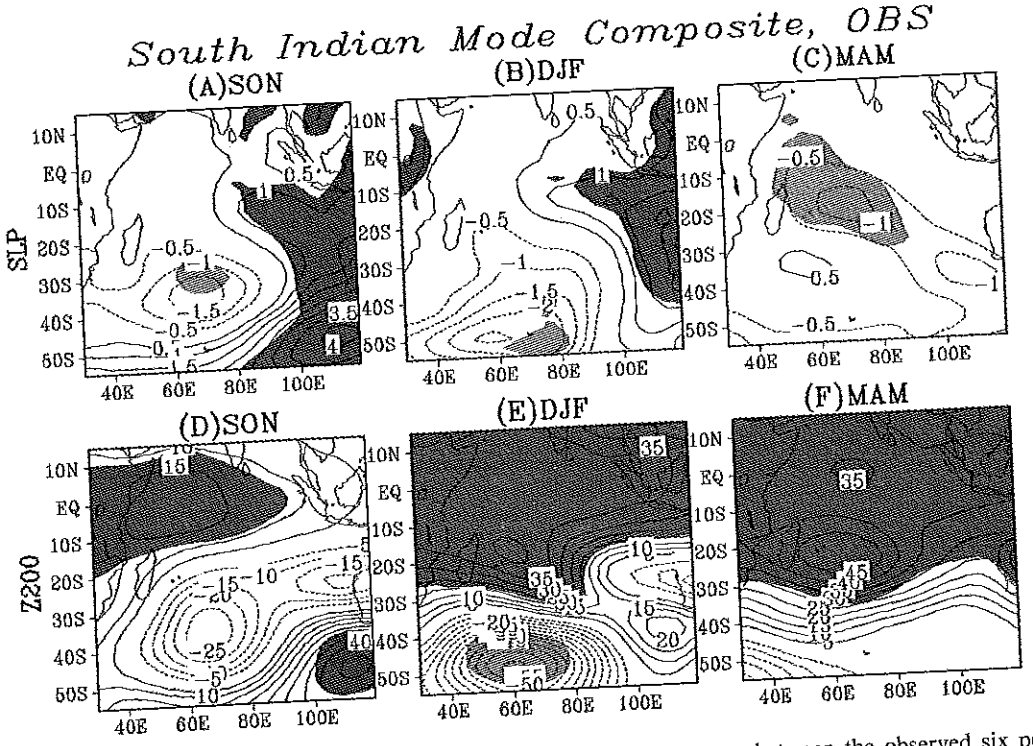

Fig. 10—The composite South Indian Ocean anomalous event formed by the difference between the observed six positive and nine negative events for the SLP (A-C) and the Z200 (D-F). The sequence of composites is from SON (A, D), to DJF (B, E), then to MAM (C, F). The contour intervals are 0.5hPa for the SLP anomalies and 5 meters for Z200, both with zero contours omitted. Regions with the differences of the SLP or Z200 anomalies above 95% significance level are shaded.

Based on these two criteria, six positive and nine negative events were chosen from the 51 winters. (They are marked in Fig.8 with closed and open circles respectively). We realize that the one standard deviation criteria is subjective. Moreover, major positive events chosen in Fig.8 tend to group in mid-fifties to mid-seventies, possibly due to a long-term modulation of the background state. However, a choice of other reasonable values does not change the results qualitatively. Following the same procedure, 41 positive and 36 negative events were chosen from the 300 DJF seasons of the CGCM simulation. With a larger sample size, the major model events are much more evenly distributed in time.

Using these major cases, typical evolutions of positive and negative events were formed by averaging for their corresponding seasons in nine-season sequences centered at the chosen DJF. A composite event was formed by the difference between the positive and negative events. The statistical significance between the differences was examined through a *students'-t* test. In general, large-scale statistically significant differences occur mostly in the period from one season before the central time of composite to one season after.

5.1 Observed composite event

Figure 9 shows the evolution of SST, surface wind stress and heat flux anomalies from SON to MAM in a composite observational IOSD event. The corresponding SLP and 200hPa geopotential height anomalies (Z200) are given in Figure 10. The dipole-like anomalous SST pattern starts to appear in SON (Fig.9A), with the positive SST anomalies forming a southeast-northwest tilting zone centered at 25°S and 70°E and a weak cold center near 45°S and 60°E-70°E. The wind stress anomalies show a pair of vortices with an anticyclonic circulation off the tropical-subtropical eastern Indian Ocean and a cyclone to its southwest, which is close to the center of the cold SST anomalies. This surface circulation pattern is consistent with the low SLP center near 40°S and 60°E-70°E and the positive SLP anomalies to its northeast and southeast (Fig.10A). To the south of 30°S, the atmospheric anomalies have a vertically equivalent barotropic structure, as shown by the similarity between the SLP (Fig.10A) and Z200 (Fig.10D) anomalies.

The northwesterly wind anomalies associated with both vortices prevail over the warm SST anomalies in

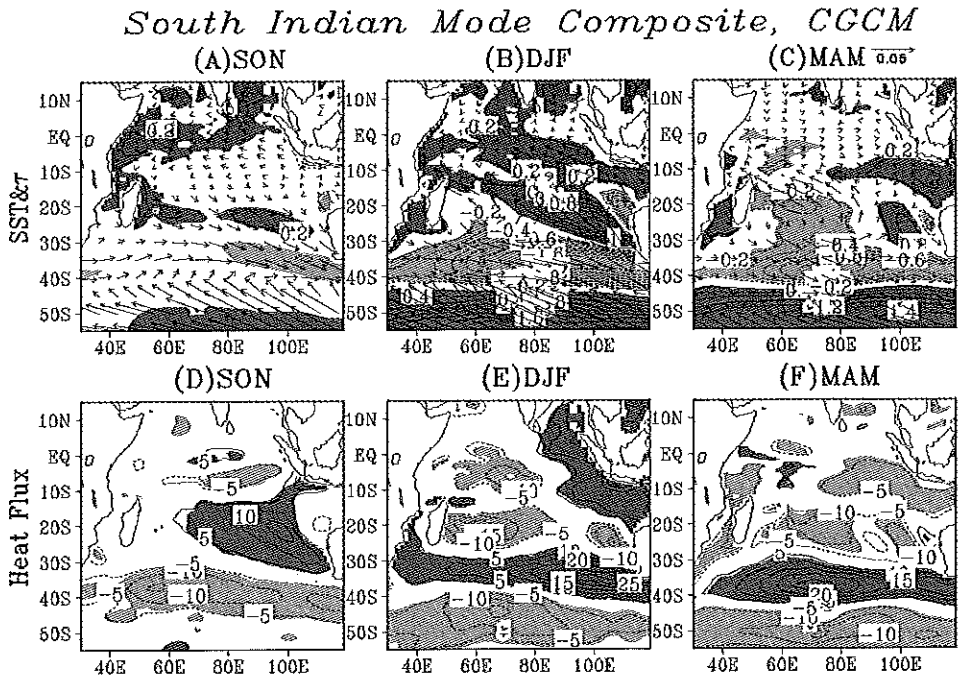

Fig. 11—The composite South Indian Ocean anomalous event formed by the difference between the 41 positive and 36 negative CGCM events for the SST and wind stress anomalies (A-C) and surface heat flux anomalies (D-F). The sequence of composites is from SON (A, D), to DJF (B, E), then to MAM (C, F). The contour intervals are 0.2°C for the SST anomalies and 5 Wm^{-2} for the surface heat flux anomalies, both with zero contours omitted. The wind stress vector magnitude of 0.05Nm^{-2} is shown at the top right of panel (C). Regions with the differences of the SST or heat flux anomalies above 95% significance level are shaded.

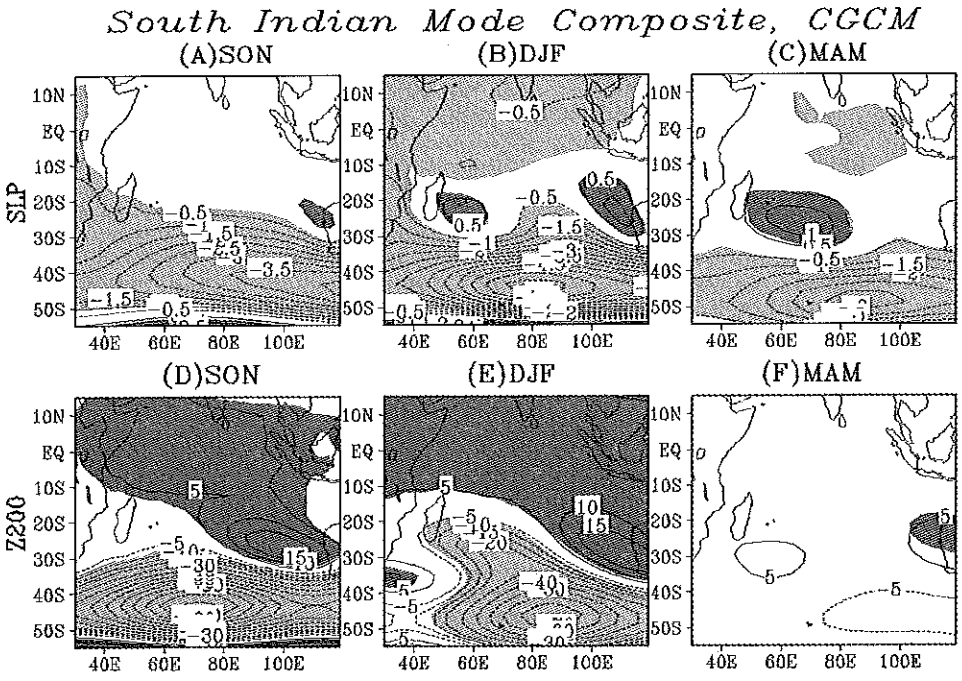

Fig. 12—The composite South Indian Ocean anomalous event formed by the difference between the 41 positive and 36 negative CGCM events for the SLP (A-C) and the Z200 (D-F). The sequence of composites is from SON (A, D), to DJF (B, E), then to MAM (C, F). The contour intervals are 0.5hPa for the SLP anomalies and 5 meters for Z200, both with zero contours omitted. Regions with the differences of the SLP or Z200 anomalies above 95% significance level are shaded.

the subtropical zone. Since these anomalies of wind stress counter the direction of the climatological seasonal trade winds in this region (Fig.2B), they reduce the total wind speed in this region. The reduced latent heat loss associated with the weaker wind speed may account for the increased anomalous surface heat flux around $10Wm^{-2}$ into the ocean between 20°S-30°S (Fig.9D) although the heat flux anomalies are not as statistically significant as the SST anomalies. In the mid-latitude zone (40°S-50°S), the easterly anomalies also counter the prevailing westerlies and play a major role of the net heat gain in the eastern part of the basin. However, a net heat loss in the western part of the basin (Fig.9D) forces the cold SST there (Fig.9A). The anomalous Ekman pumping near the center of the cyclone also enhances these cold SST anomalies.

In the subsequent season (DJF), both the anomalous low SLP (Fig.10B) and Z200 (Fig.10E) centers are shifted southward to 50°S. Associated with the shift, the wind stress anomalies reversed sign in the mid-latitude (Fig.9B). The enhanced mid-latitude westerlies should contribute to the intensification of the cold SST anomalies in the southwest through enhanced heat loss. However, the accumulative net heat flux anomalies into the ocean seem to be too small in this region (Fig.9D, E). We notice that, in this composite, the heat flux signals are generally not as significant as in other fields, possibly because the reanalyzed heat fluxes are less reliable. In the subtropical zone, the northwesterly wind stress anomalies are not only persistent but also further enhanced, which increases the warm SST anomalies in the region through sustained heat flux into the ocean (Fig.9D, E).

By MAM, the extratropical low SLP and Z200 anomalies largely disappear (Fig.10C, F). Correspondingly, the SST anomalies (Fig.9C) are also weakened because the surface heat fluxes largely turn to a damping forcing (Fig.9F). In comparison, the cold SST anomalies seem to be more persistent. So are the warm anomalies close to the northeast of Madagascar. It is interesting to note that a statistically significant low SLP center is established over the persistent warm SST anomalies (Fig.10C). At 200 hPa, a positive Z200 center is enhanced locally from the past season (Fig.10E, F). The opposite signs between the SLP and Z200 anomalies demonstrate the baroclinic structure of the atmospheric anomalies. It can be explained as an atmospheric baroclinic

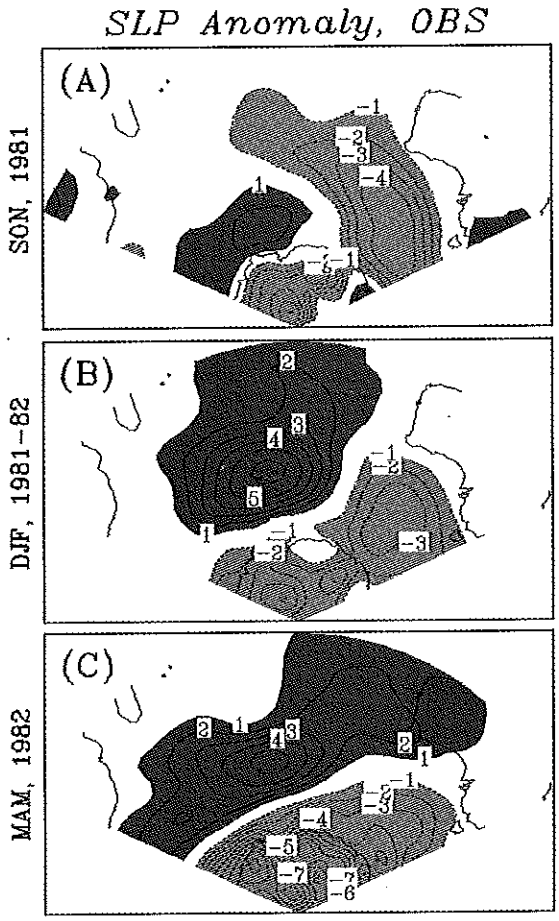

Fig. 13—The observed SLP anomalies in the Antarctica-South Indian Ocean from 20°S-90°S and 20°E-150°E for (A) SON, 1981, (B) DJF, 1981-82, and (C) MAM, 1982. The contour interval is 1hPa with zero contours omitted. Regions with SLP anomalies larger than 1hPa (less than –1hPa) are darkly (lightly) shaded.

response to the SST anomalies. We would like to point out that this is a local enhancement superimposed on the positive Z200 anomalies over the whole tropics. The latter is a part of the global response to ENSO[36]. Therefore, it is possible that, in an ENSO year, the atmospheric response to the South Indian Ocean SST anomalies makes a local contribution to the global scale ENSO signals.

5.2 CGCM composite event

The composite CGCM IOSD event is also initiated in SON with westerly to northwesterly wind anomalies between 20°S-40°S (Fig.11A), which are associated with a low pressure center to the south of Australia extending into the South Indian Ocean (Fig.12A). At 200hPa, a negative center of Z200 is

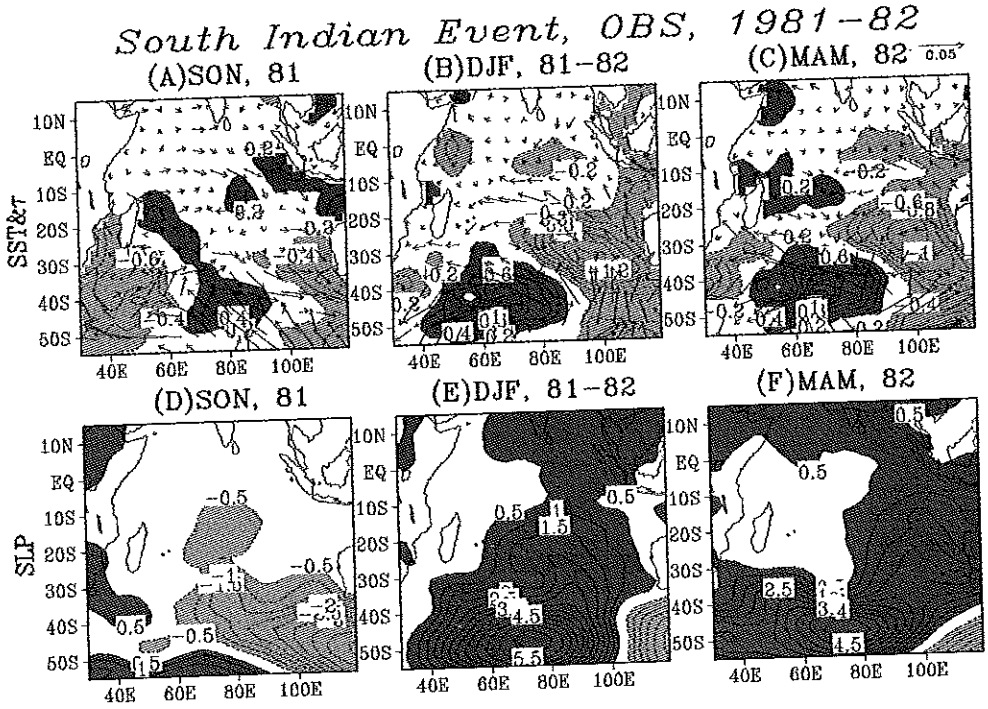

Fig. 14—The SST, wind stress (A-C) and SLP anomalies (D-F) from SON, 81 (A, D), to DJF, 81-82 (B, E), then to MAM, 83 (C, F). The contour intervals are 0.2°C for the SST anomalies and 0.5hPa for the SLP anomalies, both with zero contours omitted. The wind stress vector magnitude of 0.05Nm^{-2} is shown at the top right of panel (C). Regions with the SST anomalies larger than 0.2°C (SLP anomalies 0.5hPa) are darkly shaded. Regions with the SST anomalies less than -0.2°C (SLP anomalies -0.5hPa) are lightly shaded.

located at 45°S and 70°E (Fig.12D), to the west of the SLP center. Globally, both are a part of the global negative phase of SAM (not shown). Superimposed on the seasonal climatology (Fig.2F), the wind stress anomalies correspond to weakened (enhanced) total wind speed in the eastern subtropical (mid-latitude) ocean. These wind speed changes modulate the latent heat loss at the sea surface and generate positive heat flux anomalies in the eastern subtropics and negative ones further south (Fig.11D), which initiate the weak warm SST anomalies in the subtropical ocean and negative anomalies in the eastern mid-latitudes (Fig.11A).

More importantly, the accumulative heat flux anomalies (Fig.11D) generate the SST tendencies that lead to the enhanced SST anomalous pattern in DJF (Fig.11B), which bear significant resemblance to the heat flux pattern in the previous season. Interestingly, the positive SST anomalies also grow significantly in higher latitudes even though the local surface heat flux anomalies are negligible. This SST increase is probably generated by the southward anomalous Ekman transport associated with the easterly wind stress anomalies south of 40°S.

In DJF, the anomalous wind pattern established during last season is persistent (Fig.11B). So are the SLP centers in mid-latitudes and off Australia (Fig.12B). The center of the mid-latitude atmospheric perturbation becomes more barotropic as the SLP and Z200 (Fig.12E) anomalies are more in line with each other. On the other hand, the anomalous heat flux in DJF (Fig.11E) has become a net damping force to existing SST anomalies (Fig.11B) and generally leads to their decay in the next season (Fig.11C). The damping heat flux anomalies in MAM (Fig.11F) further weaken the SST anomalies as the wind anomalies over the eastern subtropical ocean largely disappear (Fig.11C).

An exception to this general decay occurs in the region to the east of Madagascar, where a sustained surface cooling (Fig.11E) enhances the cold SST anomalies from DJF (Fig.11B) to MAM (Fig.11C). These cold SST anomalies in turn generate a local baroclinic atmospheric response by increasing the SLP over the cold SST anomalies while producing negative Z200 anomalies at the same time (Fig.12B, E). By MAM, the local SLP anomalies grow into high-pressure center above 1hPa (Fig.12C) with an

anticyclonic surface circulation even though the upper atmospheric perturbations disappear in both the subtropics and mid-latitudes (Fig.12F).

5.3 IOSD event in 1981-82, a case study

The strong dependence of the CGCM IOSD events on SAM is largely caused by the model's inability[14] to simulate the strength of the observed ENSO cycle, which dominates the climate fluctuations globally. On the other hand, both the seasonal and interannual variability of the CGCM southern annular mode (SAM) is overly vigorous, in comparison with the observations, probably due to the inadequacy of its stabilizing mechanisms, such as the sea ice feedback, in the model. Given these factors, it is reasonable to ask how relevant the model result is to the reality.

A potential significance is that these model results provide a scenario on how the South Indian Ocean responds to the intensive atmospheric perturbations associated with the modulation of the mid-latitude westerly winds in a largely ENSO-free environment. To examine the validity of the response pattern, we have searched in the past 51-year records for similar situations. However, as one may find from Fig.8, there are only a few cases available in the past without a sizable NINO3 index value. For the major positive events, only the 1966-67 austral summer occurred in a "normal" year in the eastern tropical Pacific. On the other hand, three major negative events occurred in the DJF without significant cold SST anomalies in the NINO3 region, 1965-66, 1981-82, and 1993-94. The first case actually occurred in an El Niño year, while the latter two appeared in the normal conditions.

A preliminary examination of these events shows that the three negative events are associated with an enhancement of the meridional SLP gradient in the mid or higher latitude South Indian Ocean in SON or DJF while the opposite case occurred for the positive event. Here we use the case for 1981-82 as an example to demonstrate the process because it was contemporary to a persistent SAM episode. Figure 13 shows the anomalous SLP evolution in the South Indian Ocean sector from SON 1981 to MAM 1982. The meridional SLP gradient first appeared in the southwestern part of the sector when the negative SLP anomalies are established over Antarctica with a center of positive anomalies located further south off the coast (Fig.13A). In DJF, the positive SLP center has grown significantly and move northward to 50°S, 70°E. Its eastern flank further expands into the tropical ocean (Fig.13B). Both the negative and positive SLP anomalies persist into the MAM season (Fig.13C). The southern node was actually enhanced while the northern branch is elongated zonally through the sector. It should be noticed that the anomalous SLP structure was a part of the positive SAM episode that covered most of the Southern Ocean and Antarctica.

Given this background, we further zoom in the South Indian Ocean. A center of warm SST anomalies was formed in SON at 45°S, 70°E with cold anomalies on both sides (Fig.14A). The warm anomalies are likely forced by the weakened wind speeds (Fig.14A) associated with the SLP gradient formed between the positive SLP to the south of 50°S and negative SLP anomalies from the south of Australia intruding into the South Indian Ocean from the east (Fig.14D). In DJF, the warm SST anomalies are enhanced due to the weakening of the westerly winds in 40°S-50°S and 40°E-80°E (Fig.14B). The cold SST anomalies close to Australia also grew rapidly because of the stronger trade winds there. This evolution was caused by the high SLP anomalous center in the mid-latitude ocean and its northward extension in the eastern part of the South Indian Ocean (Fig.14E), as we have pointed out before. This process persisted into the next season (Fig.14C, F) as the SLP center maintained.

The 1981-82 case showed several interesting features that deviate from the observed composite event (Figs.9 and 10) but inline with the model one (Figs.11 and 12). First, the evolution is associated with the SLP change over the ocean without significant change of the Australian high. Second, the northward excursion of the SLP in DJF 1981-82 (Fig.14E) center in the eastern side is more similar to the model composite SLP (Fig.12B). Finally, the warming of the sea surface to the east of Madagascar in MAM (Fig.14C), together with the local minimum of the SLP anomalies (Fig.14F), is also consistent with the model composite (Fig.11C with sign reversed) but different from the observed pattern (Fig.9C). These circumstantial evidences support the idea that the model events reflect the South Indian Ocean responses to the persistent and strong SAM type forcing in this sector.

6. Conclusion

In this study, we have compared the mean, annual cycle, and interannual variability of the oceanic and

atmospheric states in the South Indian Ocean produced by a 300-year simulation of a CGCM with 51-year (1950-2000) observational datasets. It is demonstrated that the CGCM, without artificial surface flux adjustment, simulate realistically the main features of the mean annual cycles for both the SST and lower atmospheric circulation. These include the seasonal position of the 10°C and 20°C isotherms of the SST field, the seasonal migration of the South Indian Ocean subtropical high in both the meridional and zonal directions, as well as the annual fluctuation of the trade winds and mid-latitude westerly.

Interannually, the dominant model anomalous SST pattern in austral summer and fall shows some similarities to the observed pattern of the Indian Ocean subtropical dipole mode, which features the SST anomalies of opposite signs between the northeastern and southwestern parts of the ocean. The major discrepancies of the model pattern from the observed one are its overly zonal spatial structure as well as large SST anomalies in high latitudes. A composite analysis shows that both the model and observed anomalous events are generated in response to atmospheric perturbations over the subtropical and mid-latitude South Indian Ocean starting from austral spring and summer. These atmospheric disturbances modulate the surface heat flux into the ocean through the surface wind speed changes and generate SST anomalies, which usually persist into austral fall. The persistent SST anomalies in turn modify the lower atmospheric circulation in the subtropical Indian Ocean, especially the areas near Madagascar in the fall season after the initial extratropical atmospheric perturbations have decayed.

Our results show that the regional variability in the South Indian Ocean is connected to global-scale climate fluctuations. In this aspect, the model shows different features from the observations. While the extratropical atmospheric fluctuations, which initiate the ocean-atmospheric processes, are significantly correlated to the global tropical variations associated with ENSO in observations, they are strongly linked to the SAM in the model. This difference of the forcing functions partly explains the different spatial structures of the dominant SST patterns in the model and observations, as well as their distinct evolution. It originates from the model's inability to reproduce the observed intensity of the observed ENSO cycle[14] and its overly vigorous SAM. Therefore, our results suggest that further improvement of the CGCM simulation of the air-sea interactions in the South Indian Ocean depends upon the improvements of the model's ability in simulating the statistical characteristics of these larger scale climate variations, such as ENSO and SAM, not only qualitatively but also quantitatively.

There are other issues that require deeper examination. For instance, although the correlation between the observed IOSD mode and ENSO is statistically significant, the relatively moderate correlation coefficient by no means counts for all the external influences. Therefore, it is worthwhile to examine the influences of other factors, such as SAM and the Antarctic circumpolar wave[37]. Since these factors are more or less tangled with ENSO, it is important to separate their different roles and then recombine them to account for their interactions. This again requires a model to simulate these processes with certain accuracy.

It is also necessary to understand the nature of the ENSO influences in the South Indian Ocean. At present, it is not clear how the mid-latitude atmospheric fluctuations over the South Indian Ocean are physically generated by ENSO. Cook[15] argued that atmospheric planetary waves could be generated in the eastern hemisphere over the Southern Ocean by a shift of the South Indian convergence zone during an El Niño event. However, the response pattern identified from Cook's atmospheric model forced with idealized Pacific anomalous SST pattern does not match very well with the SLP pattern (Fig.6A) delineated in our study. To pinpoint the "sources" of the teleconnection, further examinations with more realistic setting will be very useful.

Finally, both the observed and CGCM composites show that the southwestern subtropical Indian Ocean to the east of Madagascar is a sensitive area to atmospheric perturbations although the local responses to the observed and model IOSD events are in opposite directions. These different outcomes may be related to the different structures of the model and observed IOSD events since the former has a stronger mid-latitude branch while the other has a subtropical branch, which may in turn be traced back to their respective global connections. One should note that the Madagascar region is also the area where a thermocline dome is located[10,14], so that the thermocline disturbances associated with the westward propagating oceanic Rossby wave signals can have significant effects on local SST. This

oceanic mechanism actually links this region to the tropical Indian Ocean dipole mode as well as the direct response to ENSO[9,10]. Some recent studies have shown the large-scale climate influences of the SST anomalies in this region[38]. How these different oceanic and atmospheric processes interact with each other in this very important region is a very interesting topic for further study.

7. Acknowledgement

The financial support of this study is provided by a joint grant from NSF, NOAA, and NASA (NSF 0332910, NOAA NA04OAR4310034 and NASA NNG04GG46G).

8. References

1 Huang B & Shukla J, Interannual SST variability in the subtropical and extratropical southern ocean, *Technical Report*, 223, Center for Ocean-Land-Atmosphere Studies (available at 4041 Powder Mill Road, Suite 302, Calverton, MD 20705, USA), 2007, pp. 20.

2 Mason S J, Sea-surface temperature-South African rainfall associations, 1910-1989. *Int. J. Climatol.*, 15 (1995) 119-135.

3 Reason C J C, & Mulenga H, Relationships between South African rainfall and SST anomalies in the southwest Indian Ocean, *Int. J. Climatol.*, 19 (1999) 1651-1673.

4 Rocha A & Simmonds I, Interannual variability of south-eastern African summer rainfall. Part II: Modelling the impact of sea-surface temperatures on rainfall and circulation, *Int. J. Climatol.*, 17 (1997) 267-290.

5 Nicholls N, Sea surface temperatures and Australian winter rainfall, *J. Climate*, 2 (1989) 965-973.

6 England M H, Ummenhofer C C & Santoso A, Interannual rainfall extremes over southwest West Australia linked to Indian Ocean climate variability, *J. Climate*, 19 (2006) 1948-1969.

7 Behera S K, & Yamagata T, Subtropical SST dipole events in the southern Indian Ocean, *Geophys. Res. Lett.*, 28 (2001) 327-330, [10.1029/2000GL011451].

8 Saji N H, Goswami B N, Vinayachandran P N & Yamagata T, A dipole mode in the tropical Indian Ocean, *Nature*, 401 (1999) 360-363.

9 Huang B & Kinter III J L, The interannual variability in the tropical Indian Ocean, *J. Geophys. Res.*, 107 C11, (2002) 3199 [doi: 10:1029/2001JC001278].

10 Xie S-P, Annamalai H, Schott F A & McCreary J P, Structure and mechanisms of South Indian Ocean climate variability, *J. Climate*, 15 (2002), 864–878.

11 Chao J, Chao Q & Lin L, The ENSO events in the tropical Pacific and dipole events in the Indian Ocean, *ACTA Meteor. Sinica*, 63 (2005) 594-602.

12 Huang B & Shukla J, On the mechanisms for the interannual variability in the tropical Indian Ocean, Part I: The role of remote forcing from tropical Pacific, *J. Climate*, 20 (2007) 2917-2936.

13 Suzuki R, Behera S K, Iizuka S & Yamagata T, Indian Ocean subtropical dipole simulated using a coupled general circulation model, *J. Geophy. Res.*, 109 (2004), [doi:10.1029/2003JC001974].

14 Huang B & Shukla J, On the mechanisms for the interannual variability in the tropical Indian Ocean. Part II: Regional processes, *J. Climate*, 20 (2007) 2937-2960.

15 Cook K H, A southern hemisphere wave response to ENSO with implications for southern Africa precipitation, *J. Climate*, 58 (2001) 2146-2162.

16 Lau N-C, & Nath M J, Coupled GCM simulation of atmosphere–Ocean variability associated with zonally asymmetric SST changes in the tropical Indian Ocean, *J. Climate*, 17 (2004) 245-265.

17 Thompson D W J & Wallace J M, Annular modes in the extratropical circulation. Part I: month-to-month variability, *J. Climate*, 13 (2000) 1000-1016.

18 Smith T M & Reynolds R W, Improved extended reconstruction of SST (1854–1997), *J. Climate*, 17 (2004) 2466–2477.

19 Kalnay E, Kanamitsu M, Kistler R, Collins W, Deaven D, Gandin L, Iredell M, Saha S, White G, Woollen J, Zhu Y, Leetmaa A, Reynolds B, Chelliah M, Ebisuzaki W, Higgins W, Janowiak J, Mo K C, Ropelewski C, Wang J, Jenne R, & Joseph D, The NCEP-NCAR 40 year reanalysis project, *Bull. Amer. Meter. Soc.*, 77 (1996) 437-471.

20 Kistler R, Kalnay E, Collins W, Saha S, White G, Woollen J, Chelliah M, Ebisuzaki W, Kanamitsu M, Kousky V, van den Dool H, Jenne R, & Fiorino M, The NCEP–NCAR 50–Year reanalysis: monthly means CD–ROM and documentation, *Bull. Amer. Meteor. Soc.*, 82 (2001) 247-267.

21 Schneider E K, Kirtman B P, Fan Y, & Zhu Z, Retrospective ENSO forecasts: The effect of ocean resolution, *Center for Ocean-Land-Atmosphere studies Technical Report*, 109, (available at 4041 Powder Mill Road, Suite 302, Calverton, MD 20705, USA), 2001, pp. 27.

22 Schopf P S & Loughe A, A reduced gravity isopycnal ocean model: Hindcasts of El Niño, *Mon. Wea. Rev.*, 123 (1995) 2839-2863.

23 Niiler P P & Kraus E B, One-dimensional models of the upper ocean, in *Modelling and prediction of the upper layers of the ocean*, edited by E.B. Kraus, (Pergamon) 1977, pp. 143-172.

24 Barnett T P & Preisendorfer R, Origins and levels of monthly and seasonal forecast skill for United States surface air temperatures determined by canonical correlation analysis, *Mon. Wea. Rev.*, 115 (1987) 1825-1850.

25 Bretherton C S, Smith C & Wallace J M, An intercomparison of methods for finding coupled patterns in climate data, *J. Climate*, 5 (1992) 541-560.

26 Xue F, Jiang D, Lang X & Wang H, Influence of the Mascarene High and Australian High on the summer monsoon in East Asia: Ensemble simulation, *Adv. Atmos. Sci.*, 20 (2003) 799-809.

27 Huang B & Shukla J, The ocean-atmospheric interactions in the tropical and subtropical Atlantic Ocean, *J. Climate*, 18 (2005) 1652-1672.

28 Wallace J M, Rasmusson E M, Mitchell T P, Kousky V E, E.S. Sarachik E S & von Storch H, On the structure and evolution of ENSO-related climate variability in the tropical Pacific: Lessons from TOGA, *J. Geophys. Res.*, 103 (1998) 14241-14260, [10.1029/97JC02905].

29 Krishnamurthy V & B. N. Goswami B N, Indian monsoon–ENSO relationship on interdecadal timescale, *J. Climate*, 13 (2001) 575-595.

30 Kinter III J L, Miyakoda K & Yang S, Recent change in the connection from the Asian Monsoon to ENSO, *J. Climate*, 14 (2002) 1203-1215.

31 Venegas S A, Mysak L A & Straub D N, Atmosphere–ocean coupled variability in the South Atlantic, *J. Climate*, 10 (1997) 2904–2920.

32 Sterl A & Hazeleger W, Coupled variability and air-sea interaction in the South Atlantic Ocean, *Clim., Dyn.*, 21 (2003) 559-571.

33 Huang B, Schopf P S & Shukla J, Intrinsic ocean-atmosphere variability in the tropical Atlantic Ocean, *J. Climate*, 17 (2004) 2058-2077.

34 Hermes J C & Reason C J C, Ocean model diagnosis of interannual coevolving SST Variability in the South Indian and South Atlantic Oceans, *J. Climate*, 18 (2005) 2864–2882.

35 Hall A & Visbeck M, Synchronous variability in the Southern Hemisphere atmosphere, sea ice, and ocean resulting from the annular mode, *J. Climate*, 15 (2002) 3043-4395.

36 Yulaeva E & Wallace J M, The signature of ENSO in global temperature and precipitation fields derived from the microwave sounding unit, *J. Climate*, 7 (1994) 1719-1736.

37 White W B, Chen S-C & Peterson R C, The Antarctic circumpolar wave: A beta effect in ocean-atmosphere coupling over the Southern Ocean, *J. Phys. Oceanogr.*, 28 (1998), 2345-2361.

38 Annamalai H, Liu P & Xie S-P, Southwest Indian Ocean SST variability: Its local effect and remote influence on Asian monsoons, *J. Climate*, 25 (2005) 4150-4167.